3D patterns in alginate hydrogel degradation spatially guide YAP nuclear translocation and hMSC osteogenic differentiation

Claudia A. Garrido[1,2], Daniela S. Garske[1], Shahrouz Amini[2], Georg N. Duda[1], Katharina Schmidt-Bleek[1], Amaia Cipitria[2,3,4]

[1] Julius Wolff Institute for Biomechanics and Musculoskeletal Regeneration, Berlin Institute for Health at Charité – Universitätsmedizin Berlin, Berlin, Germany

[2] Max Planck Institute for Colloids and Interfaces, Potsdam, Germany

[3] Group of Bioengineering in Regeneration and Cancer, Biogipuzkoa Health Research Institute, San Sebastián, Spain

[4] IKERBASQUE, Basque Foundation for Science, Bilbao, Spain

*** Correspondence:** Amaia Cipitria, amaia.cipitriasagardia@bio-gipuzkoa.eus

Keywords: 3D photopatterned hydrogel; alginate hydrogel; dual crosslinking; click crosslinking; matrix degradation; primary human mesenchymal stromal cells (hMSC); hMSC differentiation; YAP expression, YAP nuclear translocation

Abstract

Tissue engineering involves assembling functional cells tailored to perform specific functions. Biological tissues are anisotropic and present spatial gradients in architecture and composition. This study explores a novel approach to guide human mesenchymal stromal cells (hMSCs) behavior by encapsulation in photopatterned alginate hydrogels. Two different crosslinked sections, degradable (Deg) vs. non-degradable (noDeg), are created dependent on the light exposure (UV and crosslinking

with matrix metalloprotease (MMP) sensitive peptide vs. nonUV and click crosslinking). The patterned alginate hydrogels harbor a Deg phase, with cell spreading, collective cell alignment and preferential osteogenic differentiation; and a noDeg phase, with rounded cells, no preferential alignment and higher adipogenic differentiation. The previous patterns in cell behavior are observed under growth media (in absence of biochemical stimuli) and potentiated in the presence of specific conditioned media. We confirm the involvement of mechanotransduction pathways by the integrin-mediated yes-associated protein (YAP) nuclear translocation within degradable zones, while a homogeneous cytoplasmic/nuclear distribution is evident in non-degradable zones. The patterns in cell morphology are dependent on matrix degradation and integrin-binding, as no patterns are seen using an MMP-scramble peptide or no-RGD materials. Thus, 3D patterns in hydrogel degradation spatially guide YAP nuclear translocation and hMSC osteogenic differentiation. The spatial patterns in degradation bring us a step closer to mimicking the 3D anisotropy of tissues, by allowing to segregate cell behavior. This opens new opportunities for fundamental understanding of guided collective cell behavior and tissue engineering applications.

Statement of significance

Patterned materials allow to integrate multiple characteristics in a single material which better mimic the anisotropy found in tissues. The role of extracellular matrix (ECM) degradation is a crucial step in regeneration and disease. Engineered biomaterials have been used to study how degradability impacts cell behavior. This research takes a step further by spatially segregating the biophysical properties to mimic the complex ECM architecture in tissues. We aim to understand cell-matrix interaction in patterned degradable/non-degradable alginate hydrogels and the interphase between them by evaluating primary hMSC morphology, collective cell alignment and differentiation. The results advance our understanding of the cell microenvironment and tissue anisotropy, knowledge that can be applied to fundamental studies and tissue engineering applications.

1 Introduction

Human mesenchymal stromal cells (hMSCs) have proven to be a promising therapeutic technique in regenerative medicine [1]. Several features are of interest for tissue regeneration: self-renewal, clonality (proliferation from a single cell) and potency (differentiation into different cell types) [2]. However, using hMSCs as a therapeutic strategy presents various challenges, including uncontrolled differentiation within the recipient system and subsequent adverse effects [3].

Encapsulation of hMSCs in biomaterials offers a variety of options to guide and control their behavior. 3D confinement in synthetic materials enables controlling both the local interacting chemistry and physics provided to cells and thereby modulating cell response to their environment [4][5]. Hydrogels are one opportunity for such biomaterials, since their modifiable chemistry provides tunable properties and high cytocompatibility [6]. Biophysical [7] and biochemical [8] properties of hydrogels have been shown to trigger specific cell activities. Examples include the effect of the stiffness surrounding the cells [9][10][11], their viscoelasticity [12] [13], their degradability [14], their ECM interaction by adhesion ligands [15], or their ECM fiber arrangements [16]. In many cases these efforts have focused on homogeneous materials in which the cells reside. However, biomaterials in nature are not homogeneous but hierarchically structured, and provide a distinct architecture to cells.

Thus, single-phase materials can only partially provide a mimicry of the complex ECM interaction in living tissues. Native ECM is anisotropic with distinct spatially segregated properties[17]. Multiple phases in one matrix arranged in spatially discrete sections - patterned biomaterials - allow to mimic this natural ECM anisotropy, while keeping the benefits of a well-controlled synthetic material niche. The versatility of 3D patterned materials allows to control cell behavior in specific ways. For example, patterns in biomolecule presentation can spatially guide cell migration and cell alignment

[18][19]. Still, the subject of 3D patterned synthetic niches is so far under-researched, while it offers exciting new opportunities linked to the development of new manufacturing techniques.

Despite the current developments in 3D patterned biochemical cues and mechanical properties, the effect of patterns in degradation are not fully elucidated yet. Due to the recent developments on technologies of photodegradable materials [20][21] further understanding of the cell response in 3D degradable environments is required to exploit the potential of these new technologies. Most of the 3D patterned materials in degradation have been used for endothelial cell infiltration [22], vessel sprouting [23] or endothelium formation [24]. For other cell types such as hMSCs or fibroblasts, materials with patterns in degradation have been previously studied in 2D matrices [25] and in 3D in combination with patterns in stiffness, successfully guiding cell morphology [26] and stromal cell differentiation [27]. Finally, 3D photopatterning has been successful in guiding tissue formation with deterministic intestinal organoid patterning, through spatiotemporal control of matrix degradation and softening [28]).

The mechanisms underlying cell-matrix interactions in 3D degradable materials are traction forces [29] and the creation of newly opened space due to degradation [27]. It has been previously shown that degradable materials favor a spread cell morphology [30] and stromal cell osteogenic differentiation [31]. The traction forces and integrin-mediated cell interactions in degradable materials are regulated through mechanotransduction pathways. Yes-associated protein (YAP) and transcriptional coactivator with PDZ-binding motif (TAZ) represents one of such pathways and enables nuclear mediators of mechanical signals exerted by the ECM and cytoskeletal tension [32]. The activation of this pathway is linked to the integrins on the cell surface and the associated traction forces with the anchoring points in the ECM (i.e. binding motifs) [33]. YAP/TAZ expression and nuclear translocation as a consequence of cytoskeletal tension, and its effect on cell differentiation [34], cell communication [35] or cell polarization through spatial heterogeneity in YAP activation

[28] are well known. However, further links between the role of YAP/TAZ in transducing mechanical signals due to matrix degradation into cell behavior need further research.

Here we explore how hydrogels with patterns in degradation create emergent and guided patterns in cell behavior. We present a materials-based strategy to guide 3D hMSC osteogenic differentiation by 3D patterns in alginate hydrogel degradation. The study aims to understand cell-matrix interaction in degradable/non-degradable materials and the interphase between them by evaluating primary hMSC morphology, collective cell alignment and differentiation. In addition, we explore the mechanisms underlying osteogenesis *in-vitro* mediated by YAP nuclear translocation and triggered by the biophysical properties of patterned materials. The outcomes of this study improve our understanding of the cell-ECM interactions with anisotropic biophysical properties, and bring us a step closer to mimicking the 3D anisotropy of tissues. This opens new opportunities for fundamental understanding of guided collective cell behavior and biomaterial-guided tissue engineering applications.

2 Materials and Methods

2.1 Alginate modification

Norbornene and tetrazine were added to the alginate backbone via carbodiimide chemistry. The alginate used was low molecular weight, high guluronic acid sodium alginate (MW 75 kDa Pronova UP VLVG; NovaMatrix). The coupling of norbornene (N, TCI Chemicals, #N0907) and tetrazine (T, Conju-probe, #CP-6021) to the alginate molecule was performed as previously described [26]. Alginate modification with norbornene was performed with a theoretical degree of substitution (DS_{theo}) of 500. Alginate modification with tetrazine was performed with a DS_{theo} of 170 (Suppl. Table S1). NMR spectroscopy was used to determine the actual DS (DS_{actual}) (Suppl. Fig. S1). NMR measurements were performed, using a 1.5 % w/v alginate solution in deuterium oxide (64 scans;

Agilent 400 MHz Premium COMPACT equipped with Agilent OneNMR Probe) and analyzed using MestreNova Software (version 12.03).

2.2 Isolation and culture of primary human bone-marrow derived mesenchymal stromal cells (hMSCs)

hMSCs (female, 50 years, no secondary diagnosis, no co-medication) were received from the Core-Facility "Cell Harvesting" of the BIH Center for Regenerative Therapies (BCRT). The cells were isolated from metaphyseal bone marrow biopsies from patients undergoing hip replacement at the Charité - Universitätsmedizin Berlin, as previously described [36][37]. Written informed consent was given, and ethics approval was obtained from the local ethics committee/institutional review board (approval number EA2/089/20) of the Charité – Universitätsmedizin Berlin.

Briefly, the bone marrow mononuclear cell fraction and the stromal cell fraction post Ficoll-density gradient centrifugation (Histopaque 1077; Sigma-Aldrich) were quantified with an automated electrical impedance-based CASY® Cell Counter (Schaerfe System GmbH). The stromal cell-containing interphase was cultured in expansion medium: Dulbecco's Modified Eagle's Medium (DMEM low glucose, Sigma-Aldrich, #D5546), 10 % v/v fetal bovine serum (Sigma-Aldrich, #F9665), 1 % Glutamax (Gibco, #35050-038) and 1 % penicillin/streptomycin (Gibco, #15140-122). Cells were maintained in a 5 % CO_2 environment at 37 °C, medium exchanged every 2 days and passaged when 80 % confluence was achieved. For 3D encapsulation, cells were used at passage 5.

For differentiation analyses, cell-laden hydrogels were incubated in growth, osteogenic or adipogenic media. The previously described expansion media was used for growth media condition. Osteogenic medium contained: DMEM low glucose (Sigma-Aldrich, D5546) with 10 % v/v fetal bovine serum (Sigma-Aldrich, #F9665), 1 % v/v penicillin-streptomycin (Gibco, #15140-122), 50 µM ascorbic acid (Sigma-Aldrich, A5960), 10 mM ß-glycerolphosphate (Sigma-Aldrich, #G9422) and 100 nM

dexamethasone (Sigma-Aldrich, #D4902). Adipogenic medium consisted of: high glucose DMEM (Sigma-Aldrich, #D5671) with 10 % v/v fetal bovine serum (Sigma-Aldrich, #F9665), 1 % v/v penicillin-streptomycin (Gibco, #15140-122), 1 μM dexamethasone (Sigma-Aldrich, #D4902), 2 μM insulin (Sigma-Aldrich, #I6634), 500 μM 3-isobutyl-1-methylxanthine (Sigma-Aldrich, #I5879) and 100 μM indomethacin (Sigma-Aldrich, #I7378).

2.3 Hydrogel formation

Hydrogels were fabricated based on previously established protocols [26]. The single-phase materials (no photomask) were used as controls for mechanical testing of bulk properties with rheology (Section 2.4.1) and for cell stainings. In addition, patterned materials were generated as described below. For all material samples, cell culture was performed either in growth, osteogenic or adipogenic media.

2.3.1 Non-degradable matrix: Click-crosslinked hydrogels

The precursors for the hydrogel were dissolved in phosphate-buffered saline (Merck #D8537) and distributed into 2 tubes. The first tube contained norbornene-modified alginate (N-alg); MMP-sensitive (MMPsens) peptide (GCRD-VPMS ↓ MRGG-DRCG, 95 % purity; WatsonBio) at a final concentration of 5 mg/ml of hydrogel, thiolated RGD-peptide (CGGGGRGDSP; Peptide2.0) at a theoretical concentration of 5 molecules of RGD per alginate chain (DS 5, 1.2×10^{-3} mM), and the cell suspension at final concentration of 2×10^{6} cells/mL of hydrogel. The second tube contained tetrazine-modified alginate (T-alg) and the photoinitiator (Irgacure 2959; Sigma-Aldrich, #410896) at a final concentration of 3 mg/mL of hydrogel. The total final concentration of alginate was 2 % w/v at an N:T ratio of 1.5.

The two solutions were mixed by pipetting and cast onto a bottom glass plate (borosilicate glass, Filafarm, #1000185), with the casting area being restricted on three sides by glass spacers

(Marienfield, #1100420), and immediately covered with a glass slide previously treated with SigmaCoat (≥ 99.5 %; Sigma-Aldrich, #SL2) to prevent adhesion. The gel height was constrained to 2 mm by the thickness of the glass spacers. Spontaneous click-crosslinking for 60 min at room temperature (RT) and in the dark allowed the N:T covalent bonds to form. Despite MMPsens and the photoinitiator being present, these were not activated due to the lack of UV exposure. Nevertheless, the MMPsens and photoinitiator need to be present to allow for patterned materials (see Section 2.3.3).

In order to ensure a homogeneous binding of the RGD-peptide, crosslinked gels were exposed to 2 min UV light (365 nm) at 10 mW/cm^2 (Omnicure S2000) in a custom-built exposure chamber. The RGD peptide binds to the free norbornenes via thiol-ene reaction. The cylindrical hydrogels were punched from the cast gel sheet using 5 mm biopsy punches (Integra Miltex) and incubated in cell culture media at 37 °C and 5 % CO_2.

2.3.2 Degradable matrix: MMPsens peptide crosslinked hydrogels

The production of degradable materials followed the same procedure as described in Section 2.3.1, with an additional step for the MMPsens peptide crosslinking. After casting the hydrogel solution between the glass plates, the material was exposed to UV light at 10 mW/cm^2 for 10 min to initiate the coupling of the degradable MMPsens peptide to the norbornene-modified alginate via thiol-ene crosslinking. After the UV exposure, the materials were placed for an additional 50 min at RT in the dark to allow for the N:T covalent bonds to be formed. To ensure a homogenous binding of RGD, the hydrogels were exposed again to UV for 2 min. Hydrogels were punched out and incubated in cell culture media at 37 °C and 5 % CO_2.

2.3.3 Patterned materials: Photolitography patterned dual crosslinked hydrogels

The creation of patterned materials followed the same procedure as described in Section 2.3.2, with the addition of a photomask placed on top of the cover glass during the UV mediated thiol-ene coupling of the MMPsens peptide. The photomask had a pattern of straight lines with 500 µm thickness (UV light blocking sections, non-degradable matrix equivalent to 2.3.1) placed 500 µm apart (UV light permitting sections, degradable matrix equivalent to 2.3.2). After the 10 min UV exposure through the photomask, followed by 50 min at RT incubation, in which all the N-T bonds were formed and no additional grafting of MMP occurred, crosslinked gels were exposed to 2 min UV light at 10 mW/cm^2 without a photomask for homogeneous binding of the RGD-peptide.

Three additional control materials are included in this manuscript: broader degradable stripes using a different photomask, materials with a non-degradable peptide sequence and materials with no RGD adhesion peptide. All of the controls follow the procedure established under section 2.3.2. Different photomasks featured straight lines with 800 µm thickness allowing UV light through (Deg) and 200 µm UV blocking sections (noDeg). The control material with a non-degradable peptide sequence was achieved by replacing the MMPsens with the homologous scramble (MMPscr) peptide (GCRD-VpMS ↓ mRGG-DRCG, 95 % purity; WatsonBio), where the amino acids in lower case were switched for the D-isoform, unrecognizable to MMP enzymes. For the control materials with no adhesion peptides, the thiolated RGD solution was replaced with PBS.

2.4 Mechanical characterization

Mechanical characterization was performed on day 1 and day 14. All mechanical characterization was performed with cell-laden materials to quantify the effect of cell-driven enzymatic degradation of the hydrogels. The material degradation and changes in mechanical properties were evaluated via

two different methods: rheology to quantify loss and storage modulus of single-phase materials and microindentation to map the surface elastic modulus of single-phase and patterned materials.

2.4.1 Rheology

Storage and loss modulus of single-phase hydrogels were determined with a rheometer (Anton Paar MCR301) via frequency sweeps with a parallel plate geometry of 8 mm (PP08, Anton Paar). The frequency sweep was performed from 0.01 to 10 Hz and at 0.1 % shear strain at RT (n = 6). Once contact with the gel surface was established, a pre-compression of 10 % of the height of the hydrogel was applied prior to the measurement. No additional hydration was needed as the experiment lasted less than 10 min. To obtain the elastic modulus, first the shear modulus (G) was derived from the storage (G') and loss (G") modulus using Rubber's elasticity theory. The mesh size (ξ) was approximated based on storage modulus G' in low frequencies (0.1-1 Hz), as previously described [38].

2.4.2 Microindentation

To verify the patterns in mechanical properties of the 3D hydrogels, the surface elastic modulus of the materials on day 1 and day 14 was mapped into a heatmap. Similar procedures as previously described [26] were used and adapted for softer materials. Depth-sensing microindentation measurements were done using a Triboindenter TI-950 (Hysitron-Bruker, MN, USA) with a cono-spherical tip of 50 µm radius. The tip was calibrated by an air indent, followed by a quick approach to detect the surface. Then, the measurements were automatized as follows: ~350 µm retraction, an indent approach of ~150 µm and strain rate of ~30 µm/s. The measurements were done using an automated mode to map an area with 10 x 10 indents with 200 µm spacing.

To obtain the elastic modulus from the load-displacement indentation curves, the Hertzian contact model was used. Considering the high number of indents, the analysis of the load-displacement

curves was automated by a custom-made Python3 script. We used an adapted version of the script described in our previous work [26]. The adaptations were made solely on the selection of the origin point. The origin point is the initial contact point where the tip gets in contact with the material surface and from which the Hertzian model will be determined. This procedure was previously automatized by mathematically determining the minimum of the first part of the indentation curve. However, in very soft materials like the ones presented in this study, the origin point could not be identified using the previous method, as the initial contact point where the tip gets in contact with the material surface was not as clear as with stiffer gels. The adapted version of the script allows the user to select the origin point manually.

2.5 Cell viability

To verify cell viability Live/Dead stainings were performed after 1 and 14 days. The hydrogels were taken out from the incubation media and washed with PBS (Merck #D8537). Then the cells were stained with a solution of 4 µM Calcein AM (Biomol Bioquest #ABD-22002, 500x solution in DMSO) and 4 µM Ethidium homodimer-1 (Sigma #E1903, dilution 1:1000 from original solution) dissolved in PBS to identify live and dead cells, respectively. The staining solution volume was 400 µl per hydrogel in a 24 well plate, stained for 12 min in a cell culture incubator at 37 °C, 5 % CO_2 in the dark. A final washing step was performed with 400 µl of PBS per hydrogel at RT for 5 min and protected from light. Imaging was performed on a confocal microscope (Leica SP5, Germany). Quantification of cell number and viability at each time point was performed using ImageJ software (ImageJ 1.53s) [39]. One position per gel from 3 independent samples was acquired at the gel center at 10x water-immersed objective (HCX APO L U-V-I 10.0x0.30), with tile merging of 3x3.

2.6 Cell morphology

Cell morphology was assessed after 1 and 14 days, staining the nuclei and actin cytoskeleton using SYTOX and Phalloidin, respectively. All steps were performed under orbital shaking in a 24 well plate and using a volume of 500 uL per gel. The culture media was removed and the gels were washed twice with PBS (Merck #D8537). Then, the encapsulated cells were fixed in 4 % paraformaldehyde solution (Sigma-Aldrich, #158127) for 45 min at RT, followed by permeabilization with 0.3 % Triton X-100 (Sigma-Aldrich, #11488696) for 15 min, washed twice with 3 % bovine serum albumin (BSA, Sigma-Aldrich, #A7906) in PBS for 5 min. The staining solution was dissolved in PBS containing 0.1 % TritonX-100 and 3 % BSA and with the following concentrations: 0.5 µM SYTOX (Thermo Fisher, #S11381) and 1 µg/mL of Phalloidin 405 Conjugate (CruzFluor™, #SC363790). The staining was performed protected from light, during 4 h at RT. Final washing was performed twice with 3 % BSA in PBS for 5 min at RT. For imaging, three different positions per gel were acquired at the gel center from two independent samples using a confocal microscope (Leica SP5, Germany). For a general quantification of cell morphology, 10x water-immersed objective (HCX APO L U-V-I 10.0x0.30), with a tile merging of 2x2 was used.

2.7 Cell differentiation

Cell differentiation was tested using Osteocalcin (OCN) as early osteogenic differentiation marker (see Section 2.8) and OsteoImage as late osteogenic differentiation marker, and Nile Red for adipogenic differentiation. The stainings were performed after 14 days, always in combination with cell morphology staining, SYTOX and Phalloidin, described in Section 2.6.

For OsteoImage (Lonza, #PA1503) the staining procedure followed the provider´s instructions. Briefly, the fixed cells (see section 2.6) were washed with the wash buffer twice for 5 min. Then, the previously diluted 1:100 Osteoimage staining reagent in dilution buffer was added to the gels, 500 µL

per gel. The incubation was carried out at 4 °C, overnight and protected from light. The next day, the samples were washed three times with the wash buffer and then imaged.

For Nile Red staining (Thermo Fisher, #N1142), a 30 mM stock was prepared in DMSO and used as a 1:1000 dilution. The staining was performed on fixed cells (see section 2.6) at 4 °C, overnight and protected from light. The next day, the samples were washed three times with the 3 % BSA in PBS and then imaged.

For imaging, three different positions per gel were acquired at the gel center from two independent samples using a confocal microscope (Leica SP5, Germany). For a general quantification of cell morphology, 25x water-immersed objective (HCX IRAPO L 25.0x0.95), with a tile merging of 4x4 was used.

2.8 Immunostainings

YAP and Osteocalcin expression was evaluated by immunofluorescence. After performing the morphological staining, SYTOX and Phalloidin, described in Section 2.6., the primary antibody was incubated for 24 h at 4 ºC under constant rocking. The antibodies used were: YAP IgG2aκ mouse monoclonal (Santa Cruz, #sc-101199) at 10 µg/mL in PBS, and OCN Monoclonal Mouse IgG1 (R&D Systems, #MAB1419) at 25 µg/mL in PBS. After the primary antibody staining, the samples were washed three times with 400 µL of 3 % BSA in PBS for 30 min. The secondary antibody (ThermoFisher, #A32728) was stained for 2 h at RT under constant rocking. Finally, the samples were washed 3 times with 3 % BSA in PBS and imaged. For imaging, three independent positions per gel were acquired at the gel center from two independent samples using a confocal microscope (Leica SP5, Germany). For a general quantification of cell morphology, 25x water-immersed objective (HCX IRAPO L 25.0x0.95), with a tile merging of 4x4 was used.

2.9 Quantitative analysis of stained sections

The cell morphology in 3D patterned materials was evaluated using a previously described macro [26] written in ImageJ (ImageJ 1.53s). The cell projected area, cell circularity and cell number were obtained from z-stack projections. The macro offers the possibility to freely divide an image into a grid, which leads to a heat map in which the results are later depicted. To evaluate collective cell alignment, the Image J plugin Directionality was used [40]. The cell border threshold was manually established. The graphs show the 'Direction (°)' or angle, vs. the 'Amount', which shows the fraction of cells with a preferred direction, normalized to the total cell number.

YAP, Osteocalcin (OCN) and Nile Red (NR) expression was quantified as a percentage of the marker expressing cells (YAP, OCN or NR positive cells) divided by the total cell number (SYTOX). The function of "analyze particles" in Image J was used and a threshold for the markers was established using an unstained control for NR and a staining with only the secondary antibody for OCN. The mineralized area obtained with OsteoImage (OI) staining was established as a percentage by dividing the OI area by the total cell area (phalloidin staining).

The nuclear to cytoplasmic ratio of YAP was evaluated using a previously described method [41]. Briefly, individual cells were segmented for nucleus (SYTOX) and cytoplasm (phalloidin) to define the respective subcellular regions. Next, YAP average intensity within each subcellular region was quantified and the ratio calculated.

2.10 Statistical analysis

Statistical analysis was performed in GraphPad Prism 8 (version 8.4.3 for Windows, GraphPad Software Inc., Boston, Massachusetts USA). To test for normality, the Shapiro-Wilk test was applied. For normally distributed data, bar plots showing mean and standard deviation (SD) were used and the statistical comparison was performed using an ANOVA (alpha < 0.05-0.001) corrected with

Bonferroni test for multiple comparisons. For not normally distributed data, box plots with median, 1st and 3rd quartile were used and data was compared using a Kruskal-Wallis test (alpha < 0.05-0.001) corrected with Dunn´s test for multiple comparisons

3 Results

3.1 Anisotropic degradation of cell-laden patterned hydrogels leads to patterns in mechanics

Cells were encapsulated homogeneously in photopatterned alginate hydrogels (Fig. 1A) with initial homogeneous mechanical properties (Fig. 1G). The mechanical properties of cell-laden hydrogels evolved during time due to the cellular enzymatic action (Fig. 1A). Those mechanical properties were characterized by rheology (Fig. 1B-E) and microindentation (Fig. 1F-H).

The patterned enzymatic degradation of the material leads to differences in mechanics emerging 14 days after hMSC encapsulation. The degradable and non-degradable materials have close values of loss (G´) and storage (G´´) modulus on day 1 (Fig. 1B). However, on day 14 there is a pronounced difference in G´ and G´´ for Deg materials (Fig. 1C). A significant decrease over time in mechanical properties of Deg materials is observed, whereas the noDeg materials preserve their elastic modulus (Fig. 1D). The elastic modulus on day 1 of Deg (2.07 ± 0.28 kPa) is comparable to noDeg (2.03 ± 0.22 kPa). Significant differences can be seen between the elastic modulus of Deg (0.39 ± 0.27 kPa) and noDeg (1.87 ± 0.38 kPa) on day 14.

The decrease in the G´, G´´ and elastic modulus with degradation is also reflected in an increasing mesh size (Fig. 1E). The mesh size of Deg materials increases significantly between day 1 (24 ± 1 nm) and day 14 (59 ± 5 nm), whereas in noDeg materials the mesh size remains unchanged from day 1 (21 ± 0.3 nm) to day 14 (22 ± 1 nm).

Compared to the degradation behavior of single-phase materials, the corresponding phases in patterned materials show similar characteristics, as shown by the average surface elastic modulus of microindentation measurements (Fig. 1F). As seen in the representative surface map of elastic modulus, the pattern in degradation emerges over time. There is no distinct pattern of the surface elastic modulus on day 1 (Fig. 1G), with values fluctuating around 2.5 kPa, consistent with the comparable bulk elastic modulus of both single-phase materials (Fig. 1D). However, on day 14 (Fig. 1H), there are softer sections (1-1.5 kPa) corresponding to the Deg zones and stiffer sections (2.5 kPa) associated with noDeg zones.

3.2 Anisotropic hMSC morphology and collective cell alignment in 3D patterned materials

hMSCs were encapsulated in 3D anisotropic materials with patterns in degradation. The viability and cell number were evaluated in growth, osteogenic and adipogenic media using Calcein/ EtHD1 staining. Cell viability (fraction of Calcein(+) cells) remained high on day 1 (Suppl. Fig. S2D-S2F) and day 14 (Suppl. Fig. S3D-S3F) for all media used and there were no visible patterns in cell viability. Cell proliferation was also evaluated by individual quantification of the average cell number (total cells, Calcein and EtHD1). The cell number on day 1 (Suppl. Fig. S2G-S2I) remained consistent among the two phases of the patterns independent of the media used. However, the cell number on day 14 (Suppl. Fig. S3G-S3I) showed that the average number in Deg phases decreases compared to the cell number in noDeg phases. This differences in cell number could be due to the greater swelling of Deg phases (artificially reducing the cell number count per unit volume) compared to the noDeg phases.

Cell morphology was investigated in patterned materials (pattern dimensions of 500 µm:500 µm for Deg:noDeg) in growth, osteogenic or adipogenic media (Fig. 2). On day 1 (Suppl. Fig. S4), cell morphology was similar for all media and among the two phases of the material, not showing any

significant differences, neither in projected cell area nor in circularity. Patterns in cell morphology were visible on day 14 (Fig. 2), with spatially segregated differences in projected cell area and circularity. The effect seen in growth media (Fig. 2A) was enhanced in osteogenic media (Fig. 2B) and, in contrast, was less pronounced in adipogenic media (Fig. 2C).

The heat maps (Fig. 2D-2I) allowed visualization and quantification of projected cell area and circularity. Increased projected cell area (2D-2F) and decreased circularity (2G-2I) was observed in Deg regions, while cells remained round and with smaller projected cell area in noDeg zones, independent of the media. Compared to incubation in growth media (Fig. 2D, 2G), the changes in morphology were enhanced in osteogenic media (Fig. 2E, 2H) and diminished in adipogenic media (Fig. 2F, 2I). These quantitative differences and statistical analysis are summarized in the dot plots of projected cell area (Fig. 2J) and cell circularity (Fig. 2K). Finally, the Deg phases of patterned materials showed enhanced changes in cell morphology (i.e. higher cell projected area and lower circularity) compared to the Deg single phase materials (Suppl. Fig. S5E-F).

The patterned materials allowed enhanced changes in cell morphology but also differences in collective cell alignment (Fig. 3). The cell orientation was evaluated for patterns of different dimensions, 500 μm:500 μm for Deg:noDeg (Fig. 3B-I) and 800 μm:200 μm for Deg:noDeg (Fig. 3J-Q). The analysis was performed in growth and osteogenic media, since these showed the most prominent effect in hMSC morphology (Fig. 2). The first photomask dimensions, where the UV slit for the Deg material was smaller (500 μm:500 μm for Deg:noDeg, Fig. 3B-3C), resulted in aligned cells in growth media (Fig 3D) and in osteogenic media (Fig 3E). In both cases, the cells in Deg phases showed a higher tendency to orientate perpendicular to the main axis of the stripes (Fig. 3F-3H), in contrast to the cells in noDeg sections, where there was no defined orientation (Fig. 3G-3I).

However, when the UV slit in the photomask was increased and the degradable section became broader (800 μm:200 μm for Deg:noDeg, Fig. 3J-3K), collective cell alignment was lost in growth (Fig. 3L) and ostegenic media (Fig. 3M). Despite the fact that the cells were spread out in the broader Deg regions, the cells no longer showed a preferred orientation angle (Fig. 3N-3P). Despite the reduction in the stripe size of noDeg sections, there is no influence in the cell alignment and the cells remain round (Fig. 3O-3Q). The random alignment of cells in broader stripes resembles the behavior in single-phase materials (Suppl. Fig. S5A-D). This suggests that the interaction with interphases of regions with different mechanics induces collective cell alignment in degradable regions, if these interphases are detectable by the single cells; while this effect is lost with increasing distance between the interphases. This effect of collective cell alignment is highly dependent on the dimensions of the stripes, i.e. the distance between interphases of regions with different mechanics, and does not depend on the media used, growth (Fig. 3D, F, G, L, N, O) vs. osteogenic media (Fig. 3E, H, I, M, P, Q).

3.3 3D patterns in alginate hydrogel degradation spatially guide hMSC osteogenic differentiation

Previous findings showed that 3D patterns in alginate hydrogel degradation induced an anisotropic response in hMSC morphology, enhanced by biochemical cues (osteogenic media) (Fig. 2). This motivated further investigation on the anisotropic hMSC differentiation, which was evaluated by early (Osteocalcin, OCN) and late (mineralization, OsteoImage) osteogenic markers, as well as adipogenic (Nile red) markers.

The anisotropic biophysical cues provided by the patterned materials already induced spatially segregated osteogenic/adipogenic differentiation of hMSC over 14 days (Fig. 4A-C) in growth media. The early osteogenic marker (OCN) was predominantly expressed in the Deg sections (Fig.

4A), with significantly higher proportion of OCN positive cells when compared to the noDeg sections (Fig. 4G). The biophysical cues provided by the patterned materials thus created an environment for osteogenic differentiation, although mineralization (OsteoImage) was not reached in growth media alone in the first 14 days of encapsulation (Fig. 4B and 4H). In contrast to osteogenic differentiation, adipogenic differentiation occurred predominantly in the noDeg sections in growth media (Fig. 4C), where it was significantly higher when compared to Deg areas (Fig. 4I).

hMSC differentiation was further tested under osteogenic and adipogenic differentiation media. The early osteogenic marker (OCN) had higher expression in osteogenic media (Fig. 4D) compared to growth media (Fig. 4A), with a significantly higher expression in Deg phases compared to noDeg phases (Fig. 4G). Despite the biochemical stimuli of osteogenic media, the restrictive environment of noDeg sections allowed only for a low number of OCN positive cells. The late osteogenic marker (mineralization, OsteoImage) (Fig. 4E) also had higher expression in osteogenic media (Fig. 4E) compared to growth media (Fig. 4B), with significantly higher mineralized area in Deg sections compared to noDeg sections and to growth media conditions in general (Fig. 4H). Adipogenic differentiation was enhanced under adipogenic differentiation media (Fig. 4F) and significantly higher in the noDeg phase (Fig. 4I). Despite the additional biochemical stimuli (adipogenic media), the adipogenesis in the Deg phase remained under the 15 % of cells (Fig. 4I).

3.4 Anisotropic mechanosensing via YAP/TAZ signaling mediates the patterned hMSC osteogenic differentiation

After establishing the significant differences in patterned hMSC projected cell area, circularity, collective cell alignment and osteogenic differentiation, we investigated the underlying mechanism. Based on the observation of morphological changes and associated cytoskeletal tension in degradable regions, we investigated YAP expression and localization. YAP expression was evaluated in

encapsulated hMSCs in growth media (Fig. 5A) by quantifying the YAP positive expression (YAP(+)) cells (Fig. 5C) and the nuclear to cytoplasmic localization within a single cell (Fig. 5H). In growth media, the fraction of YAP(+) cells was significantly higher in Deg regions compared to noDeg (Fig. 5C) on day 14. In addition, there was a significant decrease of YAP(+) cells in noDeg areas over time from day 1 to 14, whereas a slight increase took place in Deg regions (Fig. 5C). Compared to growth media, the fraction of YAP(+) cells in osteogenic media (Fig. 5B) showed a similar correlation over time and between the two phases, but with overall increased values (Fig. 5C).

Next to YAP expression, YAP nuclear to cytoplasmic localization was analyzed in single hMSCs. In growth media, the YAP localization on day 1 is comparable in both Deg and noDeg, with nuclear to cytoplasmic expression equal to 1 (Fig. 5H). However, over time, the YAP nuclear translocation is significantly higher in Deg phase (Fig. 5D) compared to noDeg on day 14 (Fig. 5E). This is quantified in the bar plot on Figure H. The differences in YAP localization can be enhanced using osteogenic media, where the highest YAP nuclear translocation occurs on day 14 in Deg materials (Fig. 5H) and there is a small but significant increase also in noDeg materials. The nuclear translocation over time is prominent in Deg materials independent of the media used. The effect of nuclear YAP expression was enhanced in Deg phases of patterned materials compared to Deg phases in single phase materials (Suppl. Fig. S5G-J).

3.5 Matrix-bound cell adhesion peptides and degradable crosslinking peptides are required for patterned mechanosensing via YAP signaling and hMSC osteogenic differentiation

The active role of the mechanosensitive YAP/TAZ signaling pathway resulting in anisotropic hMSC morphology and osteogenic differentiation is mediated by integrin signaling. Adhesion peptides like RGD covalently bound to the matrix can stimulate cell-matrix interaction via membrane-bound integrins and induce mechanotransduction signaling pathways.

To test the relevance of integrin activation and cell-matrix interaction with alginate, we used 3D patterned alginate materials lacking RGD adhesion peptides (Fig. 6). The cells in noRGD patterned materials showed a similar behavior in the two phases on day 1 (Fig. 6A) as well as on day14 (Fig 6B). There were neither patterns in the quantification of projected cell area (Fig. 6C), nor in cell circularity (Fig. 6D) on day 14. The cell morphology comparisons between the different phases on day 1 and 14 did not show any significant differences in projected cell area (Fig. 6E) or circularity (Fig 6F). YAP expression was evaluated in Deg vs. noDeg regions on day 1 and day 14 in noRGD materials (Fig. 6G and 6H). The fraction of YAP(+) cells was lower (Fig. 6I) compared to materials with RGD (Fig. 5C) and did not vary much across regions or over time. Moreover, the YAP localization was not significantly different between regions or over time (Fig. 6J).

The role of the degradable crosslinkers is to mediate enzymatic degradation in UV exposed areas. The replacement of MMPsens peptide crosslinker with the homologous non-degradable scramble peptide (MMPscr) allowed the comparison of the degradable and non-degradable material with the same mechanical and physical properties (i.e. crosslinker length) (Fig. 7). The MMPscr patterned materials showed similar behavior at day 1 (Fig. 7A) and day 14 (Fig. 7B). There were neither patterns in projected cell area (Fig. 7C) nor in circularity (Fig. 7D) in the heat maps at day 14. Quantification of projected cell area (Fig. 7E) or circularity (Fig. 7F) did not show significant differences between the two phases at day 1 and day 14. The lack of degradation in the MMPscr regions led to a similar YAP expression (Fig. 7G) as the one seen in noDeg phases (Fig. 7H). The similarities between the two phases could be seen in the quantification of YAP (+) (Fig. 7I) and YAP localization (Fig. 7J), with no significant differences neither between phases nor over time.

4 Discussion

Assembling functional cell constructs with specific cell behavior is the core concept of tissue engineering. Patterned materials allow to integrate multiple characteristics in a single material, better mimicking the anisotropy of biological tissues. Here we explored the hypothesis that 3D patterns in hydrogel degradation can modulate cell behavior in terms of hMSC differentiation and collective cell organization. To approach this hypothesis, an alginate-based material with dual crosslinking, i.e. thiol-ene and click crosslinking, demonstrated to be a versatile platform for tuning mechanical properties and spatially segregating dynamic biophysical cues, such as degradation, in order to modulate hMSC response. The patterned material in this study offers two soft (< 3 kPa) 3D microenvironments for cells, with a comparable initial elastic modulus at day 1, and emerging patterns through degradation over time. The comparable initial elastic modulus of both phases allows a direct comparison on degradability effects, excluding other biophysical properties (i.e. matrix stiffness), which have already been studied [42][27]. The low elastic modulus (< 3 kPa) in both phases mimics the soft tissue ECM and ensures cell viability in 3D environments.

Previous results on degradable single-phase materials confirmed that the effect on cell morphology is triggered by the degradation of the MMP-sensitive crosslinking peptide [43][30]. Matrix degradation by MMPs offers the cells more space and the ability to remodel the immediate environment [44]. In our study, the spread cell morphology and lower circularity in Deg phases compared to noDeg could be attributed to the increased mesh size of the hydrogel, caused by the enzymatic cleavage of crosslinks, and absence of this in presence of MMP-scramble peptide. Our research highlighted the relevance of creating materials with patterns in degradation as anisotropic properties emerge over time and is closer to mimicking biological tissues.

The interphases of our patterned materials influenced collective cell alignment perpendicular to the stripe main axis. Cell alignment in patterned materials has been previously described on 2D topographical directed patterns [45][46][47] and in 2D mesh scaffolds [48], exhibiting a parallel

alignment to the groves/ridges, or perpendicular to them in wider curvatures (>1000µm) [49]. However, less is known about the mechanism for collective cell alignment within 3D matrices. Collective cell alignment has been evaluated showing parallel cell orientation to microengineered gelatin methacrylate hydrogels with microgrooves of < 200 µm thickness [50]. Knychala et al. showed the effect of human bone marrow cell tissue formation and organization in 3D calcium phosphate scaffolds with empty tubular pores, where the cells arranged parallel to the main axis in narrow pores (< 300µm diameter) or perpendicular to broader pores (> 400µm diameter) [51]. The perpendicular orientation to the interphases described in our research can be attributed to comparable dimensions (500 µm) and cells sensing the distinct mechanics in 3D matrices. The direct transfer of mechanisms of collective cell alignment into 3D matrices is, at this stage, mere speculation, as 3D environments offer multiple factors that can influence encapsulated cells, such as mechanical properties, adhesive ligand concentration, crosslink type and density.

In addition, the increased polymer chain flexibility due to degradation can alter the traction forces of the cells during the remodeling of the material [52]. Softening materials [53] have shown to have dynamic and adaptative traction forces during the remodeling process. The traction forces require associated focal adhesion complexes, in which the integrins interact with the RGD-binding motifs in the biomaterial [54]. This process is crucial in cell-matrix interactions that allow the cells to form filopodia [26] and activate integrin-mediated mechanotransduction signaling [55]. In our research, the materials lacking RGD showed no differences in projected cell area, circularity and lower YAP nuclear translocation between the Deg and noDeg phases, supporting importance of the matrix-bound cell adhesion peptide RGD for the cells to form focal adhesions, and allow dynamic and adaptive traction forces.

The 3D patterns in hydrogel degradation allowed spatially guided hMSC differentiation, promoting osteogenic differentiation in the Deg phase and adipogenic differentiation in the noDeg phase. Our

findings agree with previous studies on stiffness-degradation patterned materials [27], showing that the combination of stiff and noDeg environments promote adipogenesis, contrary to soft and Deg matrices fostering osteogenesis. Our study highlights the role of degradation properties on osteogenesis, since despite both regions having similar initial mechanical properties, osteogenesis occurs only in the Deg phase. Strikingly, in our study, an early osteogenesis stage could be promoted solely by biophysical factors (Deg phases in growth media). This effect could be enhanced by biochemical factors (Deg phases in osteogenic media). However, mineralization within the Deg phases was only observed after biochemical cues (osteogenic media) were added to the biophysical cues provided by the material, consistent with the literature that shows that the biomineralization is a complex process [56].

Our research describes the effect that the Deg phase has on cells, however, the cell interactions with the noDeg phase remain unknown. It was shown that some cells undergo adipogenic differentiation; however, it is still unclear what happens with the rest of the cells in the noDeg regions. The stromal cell niche suggests that the non-dynamic surroundings can contribute to preserving the naivety of stromal cells [57][58]. Furthermore, the noDeg sections also have a notable contribution to the mechanical and structural stability of the patterned material. The noDeg phases contribute to hold the Deg sections in the patterned material compared to the single Deg phase, which loses its shape by day 14 (see Suppl. Fig. S6).

It is worth mentioning the complexity of the orchestrated cell response in their respective environment. Here we explored one of the mechanotransduction pathways of how cells transduce biophysical cues (i.e. degradation and matrix softening) into a biological response (hMSC morphology and differentiation). One such process is the YAP/TAZ signaling, which involves integrin-mediated activation followed by the nuclear translocation of YAP/TAZ complex [59]. 3D hydrogels have been used to study the role of YAP/TAZ in stiff environments to mimic pathological

conditions in stiff materials (> 60 kPa) [60], and as a platform for understanding the influence of the Hippo pathway in stem cell fate [61]. Previous studies have shown that biophysical cues such as stiffness, degradation and dimensionality (2D vs 3D) can modulate the nuclear translocation of YAP/TAZ in 3D environments [34][61]. Li et al investigated the effect of single cells in 3D micropatterned arrays and associated YAP nuclear entry to nuclear morphological changes, whereby triangular or cuboid micropatterns induced nuclear compression by F-actin fibers and stretching of nuclear pores, facilitating YAP nuclear translocation [62]. In line with previous studies, hMSCs within the Deg phases of our patterned materials show a higher nuclear YAP translocation, triggered solely by the patterned degradation of the material. This effect was inhibited in noDeg phases or control (MMPscr) materials. These differences were lost in materials lacking RGD-binding motifs (noRGD), highlighting the importance of cell-matrix interactions through cell adhesion peptides.

The spatially-segregated patterned materials showed enhanced properties compared to equivalent Deg and noDeg regions in single phase materials (Suppl. Fig. S5). The Deg sections in our patterned materials could significantly enhance the spread cell morphology (with increased projected cell area and reduced circularity), induce collective cell alignment and enhance YAP nuclear translocation compared to single phase materials (Suppl. Fig. S5). The spatial patterns in degradation bring us a step closer to mimicking the 3D anisotropy of tissues.

5 Conclusions

In summary, we show that 3D patterns in alginate hydrogel degradation spatially guide YAP nuclear translocation and hMSC osteogenic differentiation. Matrix-bound cell adhesion peptide RGD and enzymatically degradable crosslinking peptides are required for patterned mechanosensing. The effects found in equivalent single-phase materials, are further enhanced in spatially-segregated patterned hydrogels. These combined results open the path to develop 3D patterned biomaterials to

mimic the anisotropy in biological tissues, for both fundamental understanding of guided collective cell behavior and tissue anisotropy, as well as biomaterial-guided tissue engineering applications.

6 Acknowledgements

The authors acknowledge the support from all group members of Cipitria, Schmidt-Bleek and Duda's laboratories. We thank the Cell Core Facility of Charité-Universitätsmedizin for providing the cells used in this study. In addition, we thank the Research Workshop at the Charité-Universitätsmedizin Berlin for developing and manufacturing some experimental devices. We thank Andreas Engels for printing the photomasks used in this research. We thank Mario Thiele from Charité-Universitätsmedizin and Samik Real from Hasso Plattner-Institute for contributing with the macros used in this research.

7 Declaration of competing interest

The authors declare that the research was conducted in the absence of any commercial or financial relationships that could be considered as a potential conflict of interest.

8 Funding

This work was funded by the Deutsche Forschungsgemeinschaft (DFG) Collaborative Research Center (CRC) 1444 grant (C.A.G, D.S.G.). A. Cipitria also acknowledges the funding from the DFG Emmy Noether grant (CI 203/2-1), IKERBASQUE Basque Foundation for Science, and from the Spanish Ministry of Science and Innovation, grant PID2021-123013OB-I00 funded by MCIN/AEI/10.13039/501100011033/FEDER, UE.

9 Data and code availability

All raw and processed data, and the MATLAB and Python scripts are available in the publicly accessible Edmond repository of the Max Planck Society: https://doi.org/10.17617/3.WLTITB

10 References

[1] M. Krampera, K. Le Blanc, Mesenchymal stromal cells: Putative microenvironmental modulators become cell therapy, Cell Stem Cell 28 (2021) 1708–1725. https://doi.org/10.1016/j.stem.2021.09.006.

[2] A.C. Wilkinson, K.J. Igarashi, H. Nakauchi, Haematopoietic stem cell self-renewal in vivo and ex vivo, Nat. Rev. Genet. 21 (2020) 541–554. https://doi.org/10.1038/s41576-020-0241-0.

[3] I. Mastrolia, E.M. Foppiani, A. Murgia, O. Candini, A.V. Samarelli, G. Grisendi, E. Veronesi, E.M. Horwitz, M. Dominici, Challenges in Clinical Development of Mesenchymal Stromal/Stem Cells: Concise Review, Stem Cells Transl. Med. 8 (2019) 1135–1148. https://doi.org/10.1002/sctm.19-0044.

[4] H.S. Kim, S.G. Kumbar, S.P. Nukavarapu, Biomaterial-directed cell behavior for tissue engineering, Curr. Opin. Biomed. Eng. 17 (2021) 100260. https://doi.org/10.1016/j.cobme.2020.100260.

[5] C.A. Deforest, K.S. Anseth, Advances in bioactive hydrogels to probe and direct cell fate, Annu. Rev. Chem. Biomol. Eng. 3 (2012) 421–444. https://doi.org/10.1146/annurev-chembioeng-062011-080945.

[6] E.C. González-Díaz, S. Varghese, Hydrogels as extracellular matrix analogs, Gels 2 (2016). https://doi.org/10.3390/gels2030020.

[7] A.M. Kloxin, C.J. Kloxin, C.N. Bowman, K.S. Anseth, Mechanical properties of cellularly responsive hydrogels and their experimental determination, Adv. Mater. 22 (2010) 3484–3494. https://doi.org/10.1002/adma.200904179.

[8] M. Guvendiren, J.A. Burdick, Engineering synthetic hydrogel microenvironments to instruct stem cells, Curr. Opin. Biotechnol. 24 (2013) 841–846. https://doi.org/10.1016/j.copbio.2013.03.009.

[9] L.R. Smith, S. Cho, D.E. Discher, Stem cell differentiation is regulated by extracellular matrix mechanics, Physiology 33 (2018) 16–25. https://doi.org/10.1152/physiol.00026.2017.

[10] C. Branco da Cunha, D.D. Klumpers, W.A. Li, S.T. Koshy, J.C. Weaver, O. Chaudhuri, P.L. Granja, D.J. Mooney, Influence of the stiffness of three-dimensional alginate/collagen-I interpenetrating networks on fibroblast biology, Biomaterials 35 (2014) 8927–8936. https://doi.org/10.1016/j.biomaterials.2014.06.047.

[11] N. Huebsch, E. Lippens, K. Lee, M. Mehta, S.T. Koshy, M.C. Darnell, R.M. Desai, C.M. Madl, M. Xu, X. Zhao, O. Chaudhuri, C. Verbeke, W.S. Kim, K. Alim, A. Mammoto, D.E. Ingber, G.N. Duda, D.J. Mooney, Matrix elasticity of void-forming hydrogels controls transplanted-stem-cell-mediated bone formation, Nat. Mater. 14 (2015) 1269–1277. https://doi.org/10.1038/nmat4407.

[12] O. Chaudhuri, L. Gu, D. Klumpers, M. Darnell, S.A. Bencherif, J.C. Weaver, N. Huebsch, H. Lee, E. Lippens, G.N. Duda, D.J. Mooney, Hydrogels with tunable stress relaxation regulate stem cell fate and activity, Nat. Mater. 15 (2016) 326–334. https://doi.org/10.1038/nmat4489.

[13] O. Chaudhuri, J. Cooper-White, P.A. Janmey, D.J. Mooney, V.B. Shenoy, Effects of extracellular matrix viscoelasticity on cellular behaviour, Nature 584 (2020) 535–546. https://doi.org/10.1038/s41586-020-2612-2.

[14] S. Khetan, M. Guvendiren, W.R. Legant, D.M. Cohen, C.S. Chen, J.A. Burdick, Degradation-mediated cellular traction directs stem cell fate in covalently crosslinked three-dimensional hydrogels, Nat. Mater. 12 (2013) 458–465. https://doi.org/10.1038/nmat3586.

[15] V. V. Rao, M.E. Wechsler, E. Cravens, S.J. Wojda, A.S. Caldwell, B.E. Kirkpatrick, S.W. Donahue, K.S. Anseth, Granular PEG hydrogels mediate osteoporotic MSC clustering via N-cadherin influencing the pro-resorptive bias of their secretory profile, Acta Biomater. 145 (2022) 77–87. https://doi.org/10.1016/j.actbio.2022.04.023.

[16] M.D. Davidson, E. Ban, A.C.M. Schoonen, M.H. Lee, M. D'Este, V.B. Shenoy, J.A. Burdick, Mechanochemical Adhesion and Plasticity in Multifiber Hydrogel Networks, Adv. Mater. 32 (2020) 1–8. https://doi.org/10.1002/adma.201905719.

[17] A. Sanchez-Rubio, V. Jayawarna, E. Maxwell, M.J. Dalby, M. Salmeron-Sanchez, Keeping It Organized: Multicompartment Constructs to Mimic Tissue Heterogeneity, Adv. Healthc. Mater. (2023) 2202110. https://doi.org/10.1002/adhm.202202110.

[18] N. Broguiere, I. Lüchtefeld, L. Trachsel, D. Mazunin, R. Rizzo, J.W. Bode, M.P. Lutolf, M. Zenobi-Wong, Morphogenesis Guided by 3D Patterning of Growth Factors in Biological Matrices, Adv. Mater. 32 (2020) 1–10. https://doi.org/10.1002/adma.201908299.

[19] C.A. DeForest, K.S. Anseth, Cytocompatible click-based hydrogels with dynamically tunable properties through orthogonal photoconjugation and photocleavage reactions, Nat. Chem. 3 (2011) 925–931. https://doi.org/10.1038/nchem.1174.

[20] T.L. Rapp, C.A. DeForest, Tricolor visible wavelength-selective photodegradable hydrogel biomaterials, Nat. Commun. 14 (2023). https://doi.org/10.1038/s41467-023-40805-w.

[21] R.M. Francis, C.A. DeForest, 4D Biochemical Photocustomization of Hydrogel Scaffolds for Biomimetic Tissue Engineering, Accounts Mater. Res. 4 (2023) 704–715. https://doi.org/10.1021/accountsmr.3c00062.

[22] B. Trappmann, B.M. Baker, W.J. Polacheck, C.K. Choi, J.A. Burdick, C.S. Chen, Matrix degradability controls multicellularity of 3D cell migration, Nat. Commun. 8 (2017) 371. https://doi.org/10.1038/s41467-017-00418-6.

[23] D. Hanjaya-Putra, K.T. Wong, K. Hirotsu, S. Khetan, J.A. Burdick, S. Gerecht, Spatial control of cell-mediated degradation to regulate vasculogenesis and angiogenesis in hyaluronan hydrogels, Biomaterials 33 (2012) 6123–6131. https://doi.org/10.1016/j.biomaterials.2012.05.027.

[24] A. Thomas, I. Orellano, T. Lam, B. Noichl, M.A. Geiger, A.K. Amler, A.E. Kreuder, C. Palmer, G. Duda, R. Lauster, L. Kloke, Vascular bioprinting with enzymatically degradable bioinks via multi-material projection-based stereolithography, Acta Biomater. 117 (2020) 121–132. https://doi.org/10.1016/J.ACTBIO.2020.09.033.

[25] A. Lueckgen, D.S. Garske, A. Ellinghaus, D.J. Mooney, G.N. Duda, A. Cipitria, Dual alginate crosslinking for local patterning of biophysical and biochemical properties., Acta Biomater. 115 (2020) 185–196. https://doi.org/10.1016/j.actbio.2020.07.047.

[26] C.A. Garrido, D.S. Garske, M. Thiele, S. Amini, S. Real, G.N. Duda, K. Schmidt-Bleek, A. Cipitria, Hydrogels with stiffness-degradation spatial patterns control anisotropic 3D cell response, Biomater. Adv. 151 (2023) 2023.01.25.525504. https://doi.org/10.1016/j.bioadv.2023.213423.

[27] S. Khetan, J.A. Burdick, Patterning network structure to spatially control cellular remodeling and stem

cell fate within 3-dimensional hydrogels, Biomaterials 31 (2010) 8228–8234. https://doi.org/10.1016/j.biomaterials.2010.07.035.

[28] N. Gjorevski, M. Nikolaev, T.E. Brown, O. Mitrofanova, N. Brandenberg, F.W. DelRio, F.M. Yavitt, P. Liberali, K.S. Anseth, M.P. Lutolf, Tissue geometry drives deterministic organoid patterning, Science (80-.). 375 (2022). https://doi.org/10.1126/science.aaw9021.

[29] L.G. Vincent, A.J. Engler, Stem cell differentiation: Post-degradation forces kick in, Nat. Mater. 12 (2013) 384–386. https://doi.org/10.1038/nmat3636.

[30] A. Lueckgen, D.S. Garske, A. Ellinghaus, D.J. Mooney, G.N. Duda, A. Cipitria, Enzymatically-degradable alginate hydrogels promote cell spreading and in vivo tissue infiltration, Biomaterials 217 (2019) 119294. https://doi.org/10.1016/j.biomaterials.2019.119294.

[31] S. Khetan, M. Guvendiren, W.R. Legant, D.M. Cohen, C.S. Chen, J.A. Burdick, Degradation-mediated cellular traction directs stem cell fate in covalently crosslinked three-dimensional hydrogels, Nat. Mater. 12 (2013) 458–465. https://doi.org/10.1038/nmat3586.

[32] S. Dupont, L. Morsut, M. Aragona, E. Enzo, S. Giulitti, M. Cordenonsi, F. Zanconato, J. Le Digabel, M. Forcato, S. Bicciato, N. Elvassore, S. Piccolo, Role of YAP/TAZ in mechanotransduction, Nature 474 (2011) 179–183. https://doi.org/10.1038/nature10137.

[33] A. Saraswathibhatla, D. Indana, O. Chaudhuri, Cell–extracellular matrix mechanotransduction in 3D, Nat. Rev. Mol. Cell Biol. (2023) 1–22. https://doi.org/10.1038/s41580-023-00583-1.

[34] N. Gjorevski, N. Sachs, A. Manfrin, S. Giger, M.E. Bragina, P. Ordóñez-Morán, H. Clevers, M.P. Lutolf, Designer matrices for intestinal stem cell and organoid culture, Nature 539 (2016) 560–564. https://doi.org/10.1038/nature20168.

[35] X. Cai, K.C. Wang, Z. Meng, Mechanoregulation of YAP and TAZ in Cellular Homeostasis and Disease Progression, Front. Cell Dev. Biol. 9 (2021) 1–12. https://doi.org/10.3389/fcell.2021.673599.

[36] S. Reinke, S. Geissler, W.R. Taylor, K. Schmidt-Bleek, K. Juelke, V. Schwachmeyer, M. Dahne, T. Hartwig, L. Akyüz, C. Meisel, N. Unterwalder, N.B. Singh, P. Reinke, N.P. Haas, H.-D. Volk, G.N. Duda, Terminally Differentiated CD8 + T Cells Negatively Affect Bone Regeneration in Humans, Sci. Transl. Med. 5 (2013) 177ra36-177ra36. https://doi.org/10.1126/scitranslmed.3004754.

[37] A. Andrzejewska, R. Catar, J. Schoon, T.H. Qazi, F.A. Sass, D. Jacobi, A. Blankenstein, S. Reinke, D. Krüger, M. Streitz, S. Schlickeiser, S. Richter, N. Souidi, C. Beez, J. Kamhieh-Milz, U. Krüger, T. Zemojtel, K. Jürchott, D. Strunk, P. Reinke, G. Duda, G. Moll, S. Geissler, Multi-Parameter Analysis of Biobanked Human Bone Marrow Stromal Cells Shows Little Influence for Donor Age and Mild Comorbidities on Phenotypic and Functional Properties, Front. Immunol. 10 (2019) 1–24. https://doi.org/10.3389/fimmu.2019.02474.

[38] S.T. Koshy, R.M. Desai, P. Joly, J. Li, R.K. Bagrodia, S.A. Lewin, N.S. Joshi, D.J. Mooney, Click-Crosslinked Injectable Gelatin Hydrogels, Adv. Healthc. Mater. 5 (2016) 541–547. https://doi.org/10.1002/adhm.201500757.

[39] C.A. Schneider, W.S. Rasband, K.W. Eliceiri, NIH Image to ImageJ: 25 years of image analysis, Nat. Methods 9 (2012) 671–675. https://doi.org/10.1038/nmeth.2089.

[40] Z.Q. Liu, Scale space approach to directional analysis of images., Appl. Opt. 30 (1991) 1369–1373. https://doi.org/10.1364/AO.30.001369.

[41] J.B. Kelley, B.M. Paschal, Fluorescence-based quantification of nucleocytoplasmic transport, Methods 157 (2019) 106–114. https://doi.org/10.1016/j.ymeth.2018.11.002.

[42] M. Bao, J. Xie, N. Katoele, X. Hu, B. Wang, A. Piruska, W.T.S. Huck, Cellular Volume and Matrix Stiffness Direct Stem Cell Behavior in a 3D Microniche, ACS Appl. Mater. Interfaces 11 (2019) 1754–1759. https://doi.org/10.1021/acsami.8b19396.

[43] S.B. Anderson, C.C. Lin, D. V. Kuntzler, K.S. Anseth, The performance of human mesenchymal stem cells encapsulated in cell-degradable polymer-peptide hydrogels, Biomaterials 32 (2011) 3564–3574. https://doi.org/10.1016/j.biomaterials.2011.01.064.

[44] K.T. Campbell, R.S. Stilhano, E.A. Silva, Enzymatically degradable alginate hydrogel systems to deliver endothelial progenitor cells for potential revasculature applications, Biomaterials 179 (2018) 109–121. https://doi.org/10.1016/j.biomaterials.2018.06.038.

[45] D.M. Le, K. Kulangara, A.F. Adler, K.W. Leong, V.S. Ashby, Dynamic topographical control of mesenchymal stem cells by culture on responsive poly(Ïµ-caprolactone) surfaces, Adv. Mater. 23 (2011) 3278–3283. https://doi.org/10.1002/adma.201100821.

[46] S. Li, Y. Sun, Y. Chen, J. Lu, G. Jiang, K. Yu, Y. Wu, Y. Mao, H. Jin, J. Luo, S. Dong, B. Hu, Y. Ding, A. Liu, Y. Shen, G. Feng, S. Yan, Y. He, R. Yan, Sandwich Biomimetic Scaffold Based Tendon Stem/Progenitor Cell Alignment in a 3D Microenvironment for Functional Tendon Regeneration, ACS Appl. Mater. Interfaces 15 (2023) 4652–4667. https://doi.org/10.1021/acsami.2c16584.

[47] M. Ventre, F. Causa, P.A. Netti, Determinants of cell-material crosstalk at the interface: Towards engineering of cell instructive materials, J. R. Soc. Interface 9 (2012) 2017–2032. https://doi.org/10.1098/rsif.2012.0308.

[48] K.O. Okeyo, Y. Kibe, T. Adachi, Controlling macroscale cell alignment in self-organized cell sheets by tuning the microstructure of adhesion-limiting micromesh scaffolds, Mater. Today Adv. 12 (2021) 100194. https://doi.org/10.1016/j.mtadv.2021.100194.

[49] M. Werner, N.A. Kurniawan, G. Korus, C.V.C. Bouten, A. Petersen, Mesoscale substrate curvature overrules nanoscale contact guidance to direct bone marrow stromal cell migration, J. R. Soc. Interface 15 (2018). https://doi.org/10.1098/rsif.2018.0162.

[50] H. Aubin, J.W. Nichol, C.B. Hutson, H. Bae, A.L. Sieminski, D.M. Cropek, P. Akhyari, A. Khademhosseini, Directed 3D cell alignment and elongation in microengineered hydrogels, Biomaterials 31 (2010) 6941–6951. https://doi.org/10.1016/j.biomaterials.2010.05.056.

[51] J. Knychala, N. Bouropoulos, C.J. Catt, O.L. Katsamenis, C.P. Please, B.G. Sengers, Pore geometry regulates early stage human bone marrow cell tissue formation and organisation, Ann. Biomed. Eng. 41 (2013) 917–930. https://doi.org/10.1007/s10439-013-0748-z.

[52] M. Colasurdo, E.B. Nieves, M.A. Fernández-Yagüe, C. Franck, A.J. García, Adhesive peptide and polymer density modulate 3D cell traction forces within synthetic hydrogels, Biomaterials 288 (2022). https://doi.org/10.1016/j.biomaterials.2022.121710.

[53] I.B. Bischofs, S.A. Safran, U.S. Schwarz, Elastic interactions of active cells with soft materials, Phys. Rev. E - Stat. Nonlinear, Soft Matter Phys. 69 (2004) 1–17. https://doi.org/10.1103/PhysRevE.69.021911.

[54] A.D. Rape, W.H. Guo, Y.L. Wang, The regulation of traction force in relation to cell shape and focal adhesions, Biomaterials 32 (2011) 2043–2051. https://doi.org/10.1016/j.biomaterials.2010.11.044.

[55] Z. Sun, S.S. Guo, R. Fässler, Integrin-mediated mechanotransduction, J. Cell Biol. 215 (2016) 445–456. https://doi.org/10.1083/jcb.201609037.

[56] M. Murshed, Mechanism of bone mineralization, Cold Spring Harb. Perspect. Med. 8 (2018) 1–11. https://doi.org/10.1101/CSHPERSPECT.A031229.

[57] C.M. Kolf, E. Cho, R.S. Tuan, Mesenchymal stromal cells. Biology of adult mesenchymal stem cells: Regulation of niche, self-renewal and differentiation, Arthritis Res. Ther. 9 (2007) 1–10. https://doi.org/10.1186/ar2116.

[58] D.B. Gomes, A. Filipa, H. Lourenço, C. Tomasina, B. Chömpff, H. Liu, N. Bouvy, S. Camarero-Espinosa, L. Moroni, D.B.G. Author, A.H.F.L. Author, C.T. Author, B.C. Author, L.H. Author, 3D soft hydrogels induce human mesenchymal stem cells "deep" quiescence, (2021) 1–54. https://doi.org/10.1101/2021.03.11.434638.

[59] I.M. Moya, S.A. Castaldo, L. Van den Mooter, S. Soheily, L. Sansores-Garcia, J. Jacobs, I. Mannaerts, J. Xie, E. Verboven, H. Hillen, A. Algueró-Nadal, R. Karaman, M. Van Haele, W. Kowalczyk, M. De Waegeneer, S. Verhulst, P. Karras, L. van Huffel, L. Zender, J.-C. Marine, T. Roskams, R. Johnson, S. Aerts, L.A. van Grunsven, G. Halder, Peritumoral activation of the Hippo pathway effectors YAP and TAZ suppresses liver cancer in mice, Science (80-.). 366 (2019) 1029–1034. https://doi.org/10.1126/science.aaw9886.

[60] G. Brusatin, T. Panciera, A. Gandin, A. Citron, S. Piccolo, Biomaterials and engineered microenvironments to control YAP/TAZ-dependent cell behaviour, Nat. Mater. 17 (2018) 1063–1075. https://doi.org/10.1038/s41563-018-0180-8.

[61] S.R. Caliari, S.L. Vega, M. Kwon, E.M. Soulas, J.A. Burdick, Dimensionality and spreading influence MSC YAP/TAZ signaling in hydrogel environments, Biomaterials 103 (2016) 314–323. https://doi.org/10.1016/j.biomaterials.2016.06.061.

[62] Y. Li, Z. Zhong, C. Xu, X. Wu, J. Li, W. Tao, J. Wang, Y. Du, S. Zhang, 3D micropattern force triggers YAP nuclear entry by transport across nuclear pores and modulates stem cells paracrine, Natl. Sci. Rev. 10 (2023). https://doi.org/10.1093/nsr/nwad165.

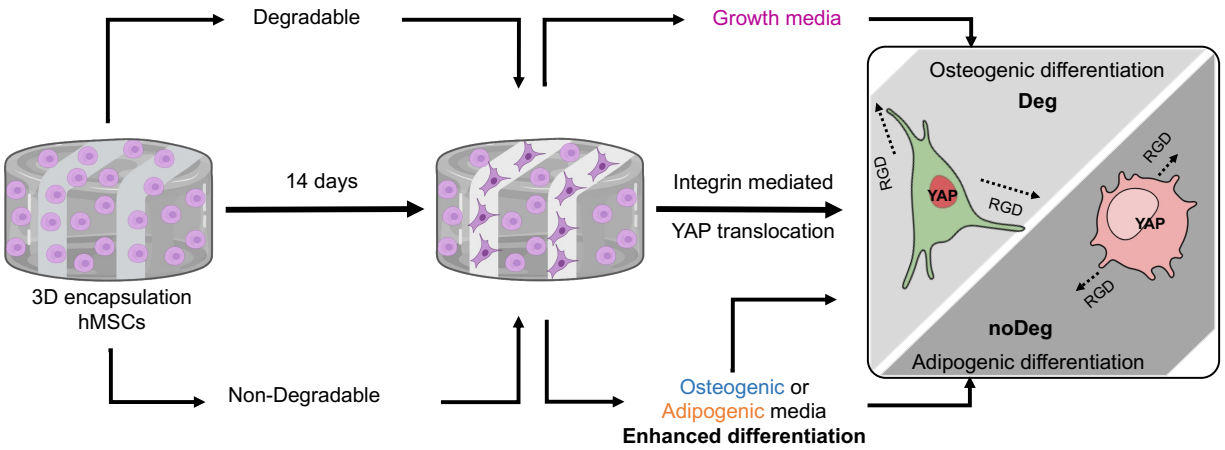

Figure 0: Graphical abstract

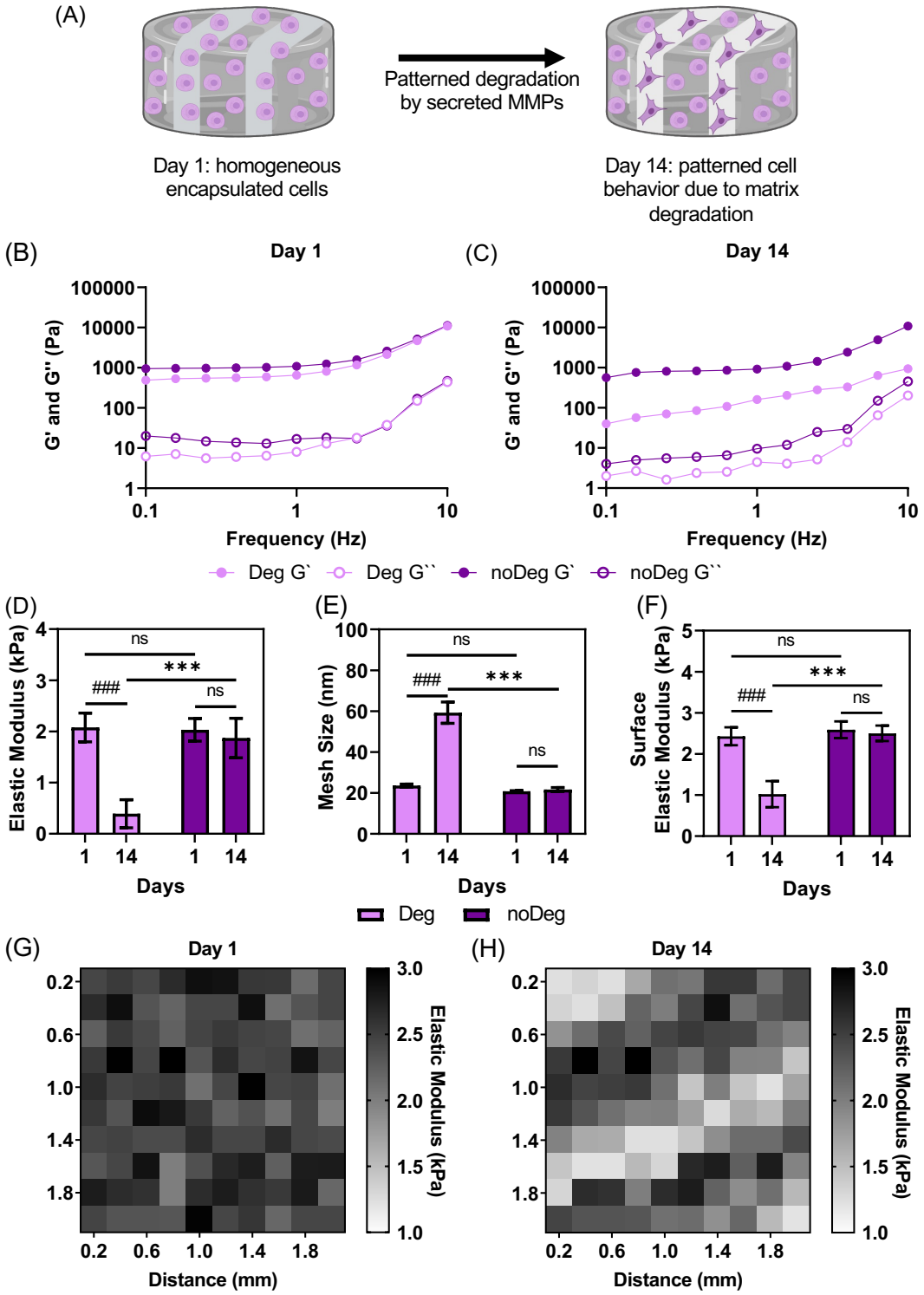

Figure 1: Mechanical characterization of cell-laden patterned materials. Sketch of the degradation of patterned materials over time due to cell-derived enzymatic action (A). Representative plots of G´ (storage modulus, ●) and G´´ (loss modulus, ○) obtained by rheology of noDeg single-phase (dark purple) and Deg single-phase (light purple) materials, on day 1 (B) and day 14 (C). Elastic modulus (D) and corresponding mesh size (E), approximated from rheology data. Surface elastic modulus in Deg and noDeg phases obtained by microindentation and averaging all indents in a specific region of patterned materials on day 1 and day 14 (F). Representative microindentation map of the surface of patterned materials as a visual illustration of the indentation elastic modulus on day 1 (G) and day 14 (H), 10x10 grid, indentation spacing of 200 µm. Bar graphs show the mean and standard deviation from n = 6 gels (D, E) and n = 11 indents per phase from 1 gel per time point (F). Statistical significance with ANOVA and Bonferroni correction (***/### = $p < 0.001$, with * for comparison of materials and # for comparison of time points).

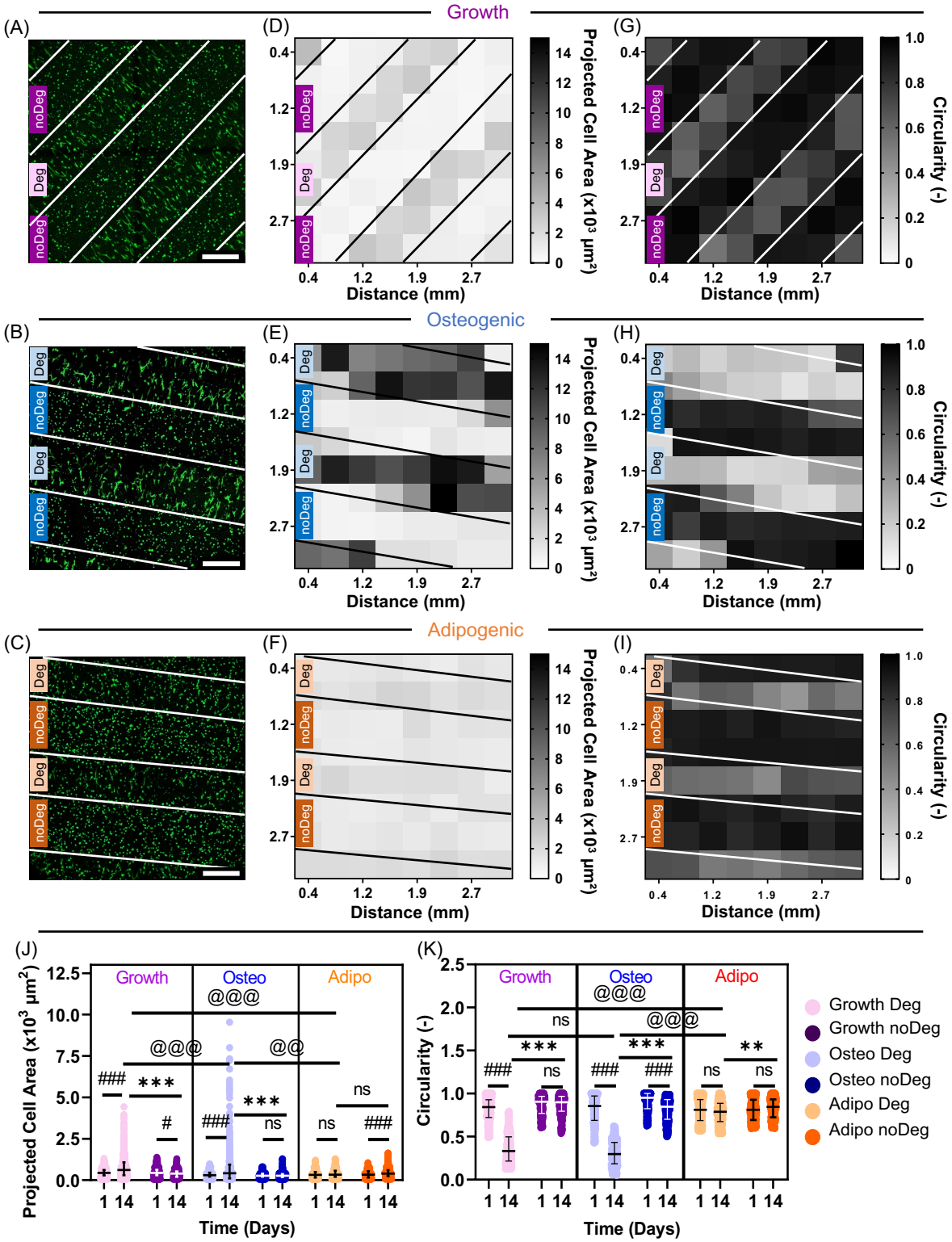

Figure 2: Cell morphology of encapsulated hMSCs in patterned materials on day 14. Representative confocal images of actin (Phalloidin/green) and nucleus (SYTOX/cyan) staining of patterned materials with hMSCs in growth (A), osteogenic (B) and adipogenic (C) media with 25x magnification, 2x2 tile merging and 250 µm z-stack. Heatmap quantification of projected cell area, with an 8x8 grid in growth (D), osteogenic (E) and adipogenic (F) media. Heatmap quantification of cell circularity with an 8x8 grid in growth (G), osteogenic (H) and adipogenic (I) media. Dot graph of raw data (> 400 single cells per phase and condition) of projected cell area (J) and circularity (K) on day 14 (see Suppl. Fig. S4 for corresponding images and heat maps on day 1). Dot graphs show the median and interquartile range of cells from n = 6 images. Statistical significance with Kruskal-Wallis and Dunn's correction (*/#/@ = $p < 0.05$, **/##/@@ = $p < 0.01$, ***/###/@@@ = $p < 0.001$, with * for comparison of materials, # for comparison of time points and @ for comparison of media). Scale bar: 500 µm.

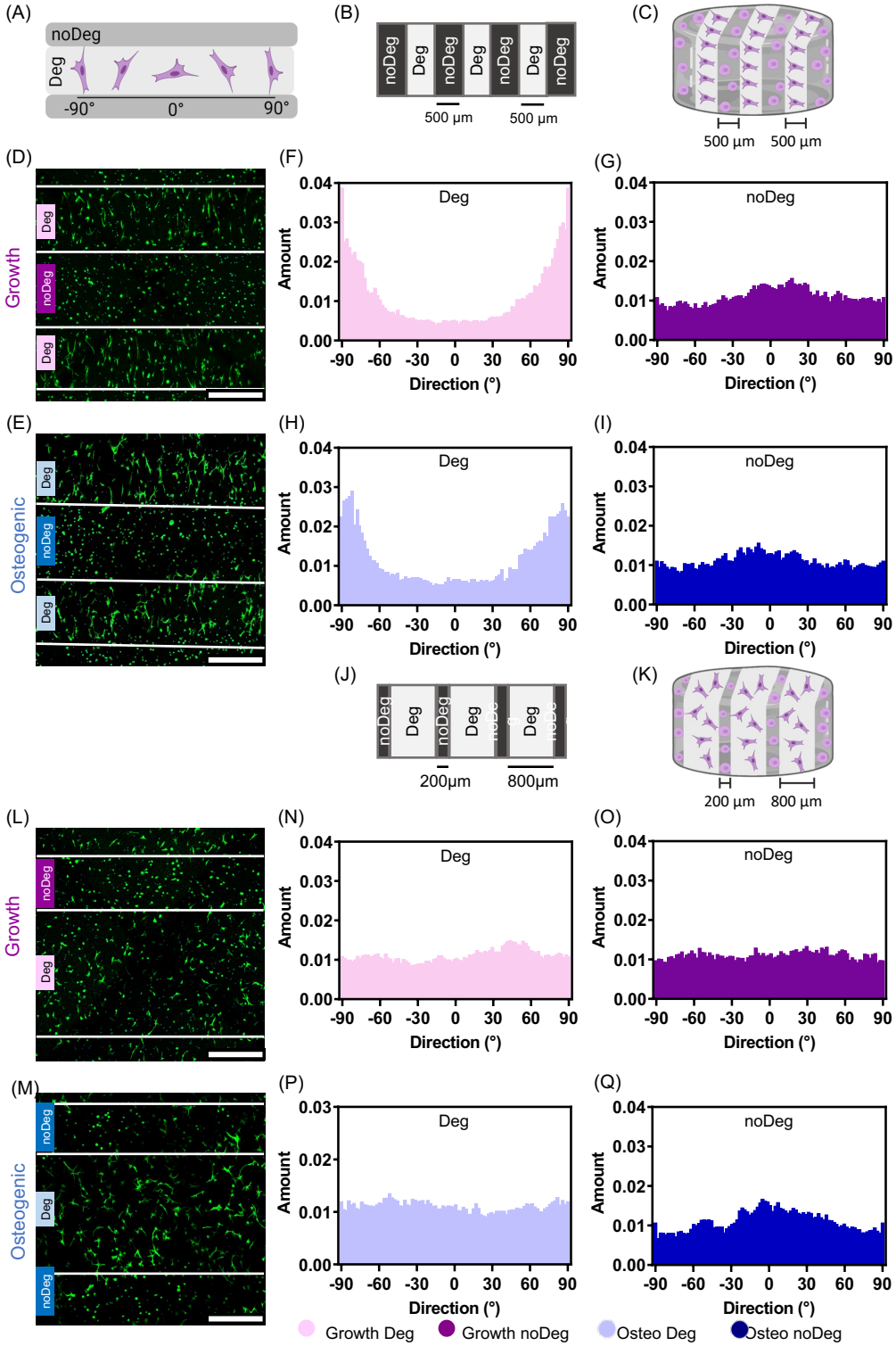

Figure 3: Collective cell alignment of encapsulated hMSCs in patterned materials on day 14 with different photomask dimensions resulting in interphases in mechanics with varying distance. Sketch of the cell angle relative to the stripe main axis and interphase direction (with 0º parallel and (+/-) 90º perpendicular to the interphase) (A). Patterned materials fabricated with photomasks of different dimensions: 500 □m:500 □m for Deg:noDeg (B, C) and 800 □m:200 □m for Deg:noDeg (J, K). Representative confocal images of actin (Phalloidin/green) and nucleus (SYTOX, cyan) staining of patterned materials with hMSCs with 500 □m:500 □m stripes in growth media (D) and osteogenic media (E), with 25x magnification, 2x2 tile merging and 250 µm z-stack. Analogous analysis in materials with 800 □m:200 □m stripes in growth media (L) and osteogenic media (M). Histograms indicating the distribution of the collective cell alignment angle in Deg and noDeg phases of materials patterned with 500:500 (F- I) and 800:200 pattern mask (N-Q), in growth and osteogenic media (n > 200 cells per phase and media). Scale bar: 500 µm.

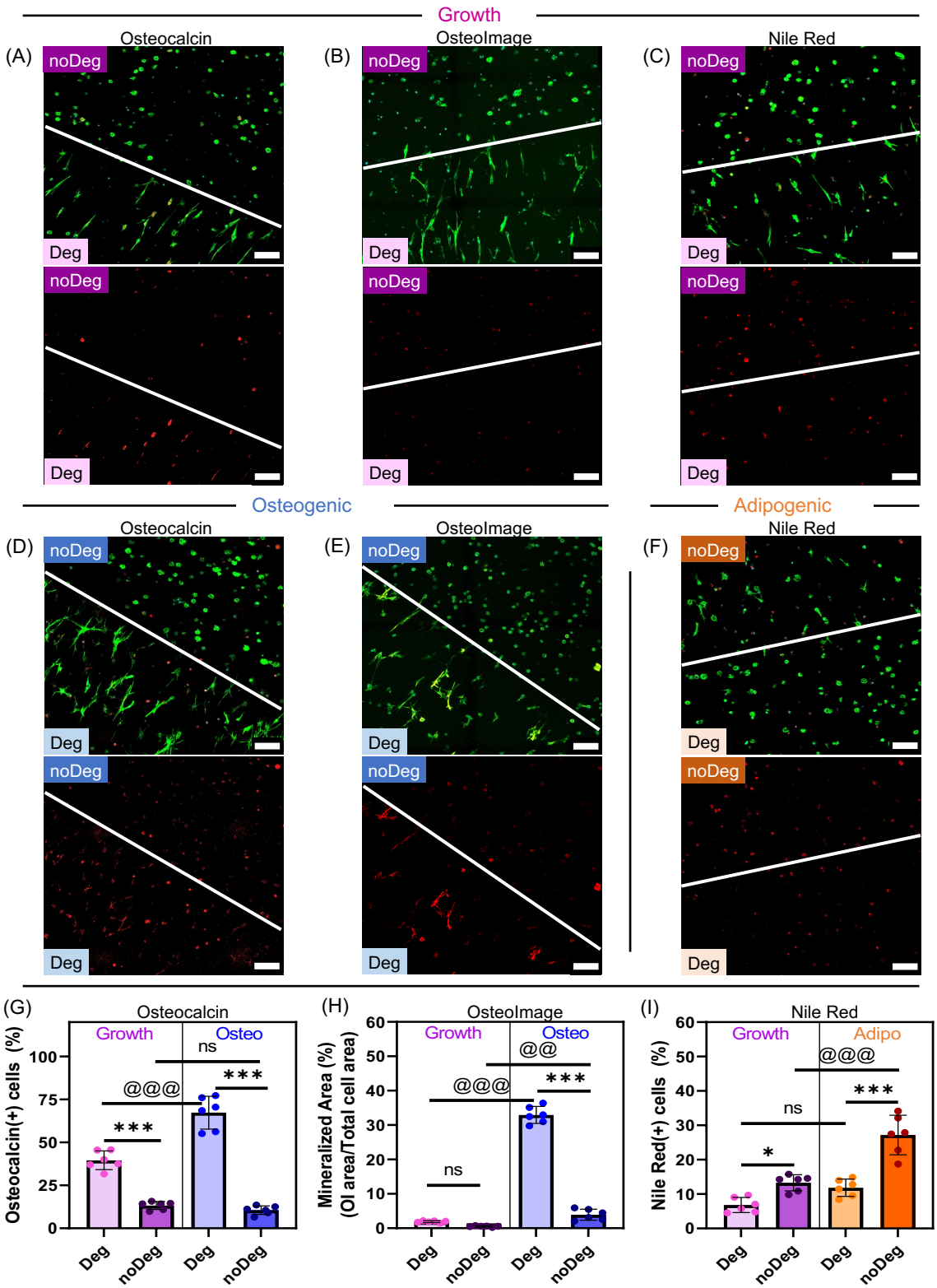

Figure 4: Osteogenic and adipogenic differentiation of encapsulated hMSCs in patterned materials on day 14. Actin (Phalloidin/green) and nucleus (SYTOX/cyan) staining with Osteocalcin (red, A, D), OsteoImage (OI, red, B, E) and Nile Red (red, C, F), in growth (A-C), osteogenic (D-E) and adipogenic (F) media. Close ups of the interphase were taken from images with 25x magnification, 4x4 tile merging, 250 µm z-stack. Comparison of Osteocalcin (G), OsteoImage (H) and Nile Red (I) quantification for Deg and noDeg phases in growth, osteogenic and adipogenic media. Bar plots show the mean and standard deviation of n = 6 fields of view containing multiple cells (n ≥ 150 cells per phase and condition). Statistical significance with ANOVA and Bonferroni correction (*/@ = $p < 0.05$, **/@@ = $p < 0.01$, ***/@@@ = $p < 0.001$, with * for comparison of materials and @ for comparison of media). Scale bar: 100 µm.

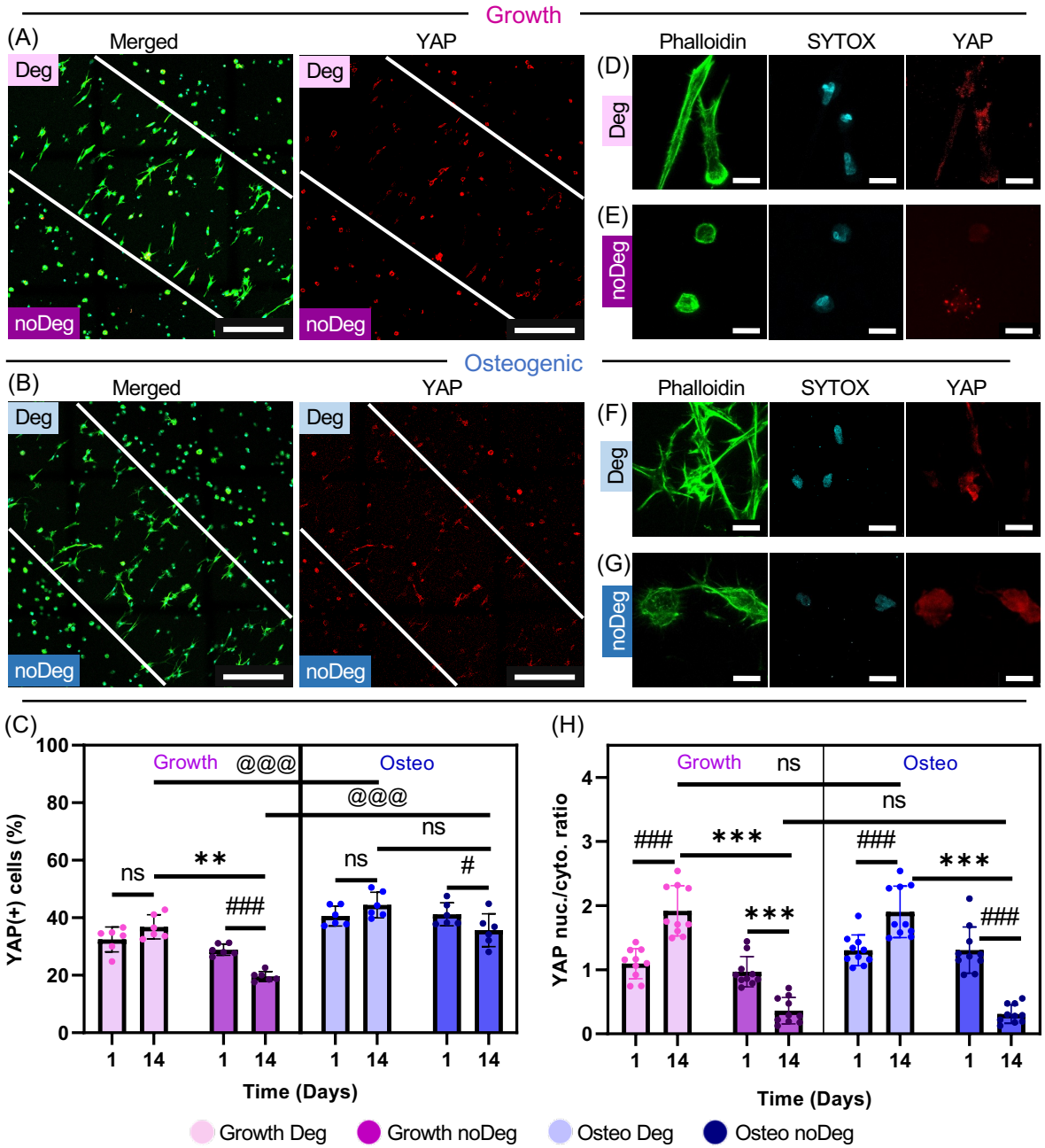

Figure 5: YAP expression and nuclear to cytoplasmic localization of encapsulated hMSCs in patterned materials on day 14. hMSC staining with actin (Phalloidin/green), nucleus (SYTOX/cyan) and YAP expression (red), in growth (A) and osteogenic (B) media, 25x magnification, 4x4 tile merging and 250 µm z-stack. Single cell images in growth media for Deg (D) and noDeg regions (E), and in osteogenic media for Deg (F) and noDeg regions (G), zoom-in, 40x magnification. Quantification of the fraction of YAP(+) cells (C) and YAP localization measured as the ratio of nuclear to cytoplasmic expression (H). Bar plots show the mean and standard deviation of n = 6 fields of view containing n > 120cells (C) and of n = 10 representative single cells from Deg vs. noDeg regions (H). Statistical significance with ANOVA and Bonferroni correction (*/@ = $p < 0.05$, **/@@ = $p < 0.01$, ***/@@@ = $p < 0.001$, with * for comparison of materials and @ for comparison of media). Scale bar: 250 µm (A, B) and 25 µm(D-G).

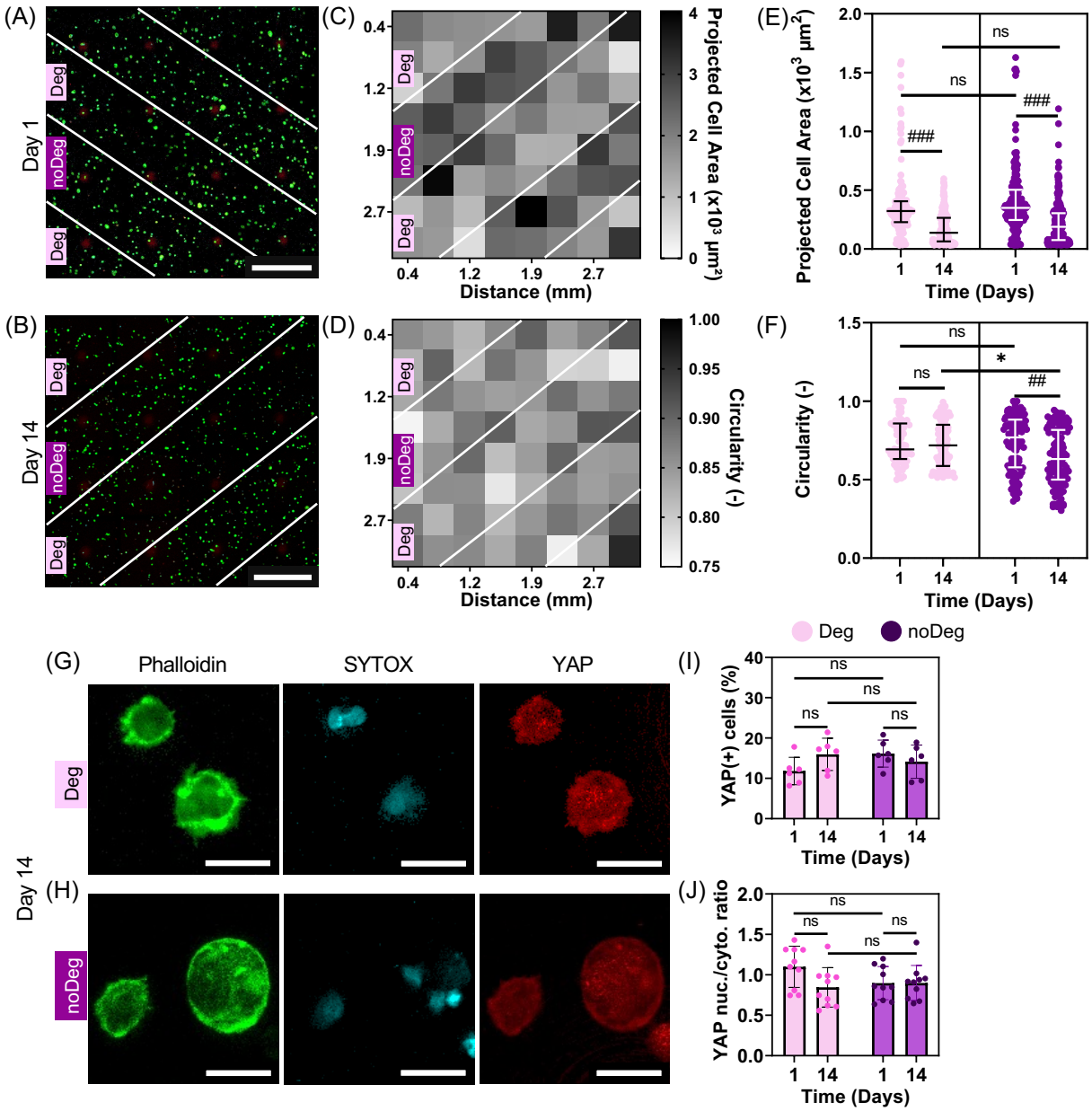

Figure 6: hMSC morphology, YAP expression and localization in patterned materials without RGD on day 1 and day 14 (growth media). Actin (Phalloidin/green) and nucleus (SYTOX/cyan) staining of encapsulated cells on day 1 (A) and day 14 (B), 4x4 tile merging with 25x magnification, 250 µm z-stack. Heat maps of projected cell area (C) and circularity (D) on day 14 corresponding to the image in (B). Dot graph of raw data (n > 400 single cells) of projected cell area (E) and circularity (F) on day 1 and day 14. Single cell images from Deg (G) and noDeg regions (H), stained for actin (Phalloidin/green), nucleus (SYTOX/cyan) and YAP expression (red), zoom-in, 40x magnification. Quantification of the fraction of YAP(+) cells (I) and YAP localization measured as the ratio of nuclear to cytoplasmic expression (J). Bar plots show the mean and standard deviation of n = 6 fields of view containing n > 120 cells (I) and of n = 10 representative single cells from Deg vs. noDeg regions (J). Statistical significance with Kruskall-Wallis and Dunn's correction in (E, F) (*/# = $p < 0.05$) and with ANOVA and Bonferroni correction in (I, J) (*/# = $p < 0.05$, **/## = $p < 0.01$, ***/### = $p < 0.001$, with * for comparison of materials and # for comparison of time points). Scale bar: 500 µm (A, B), 20 µm (G, H).

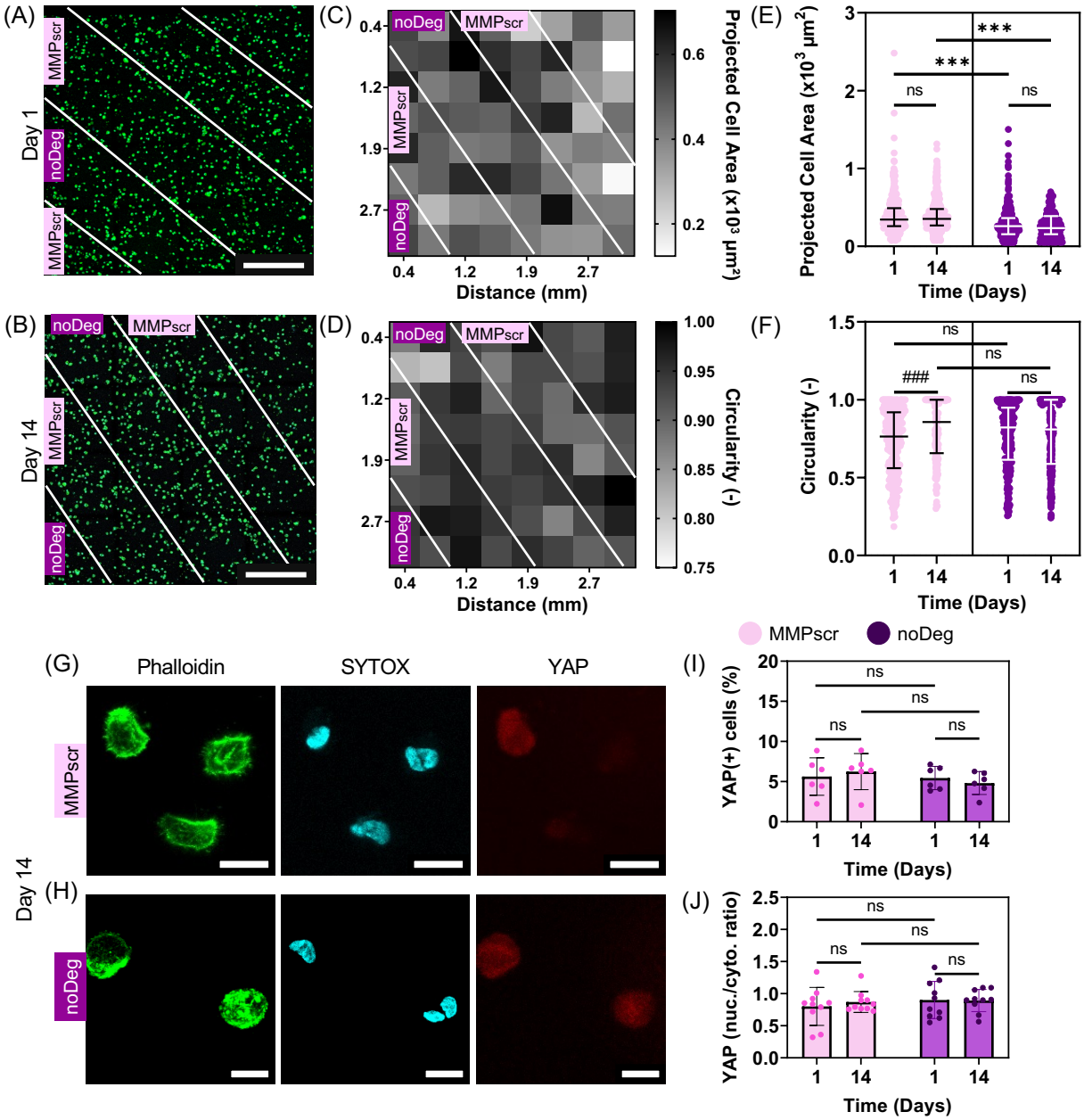

Figure 7: hMSC morphology, YAP expression and localization of encapsulated hMSCs in patterned materials with MMP scramble peptide (MMPscr) on day 1 and day 14 (growth media). Actin (Phalloidin/green) and nucleus (SYTOX/cyan) staining of encapsulated cells on day 1 (A) and day 14 (B), 4x4 tile merging with 25x magnification, 250 µm z-stack. Heat maps of projected cell area (C) and circularity (D) on day 14 corresponding to the image in (B). Dot graph of raw data (n > 400 single cells) of projected cell area I and circularity (F) on day 1 and day 14. Single cell images from MMP scramble peptide (MMPscr) (G) and noDeg regions (H), stained for actin (Phalloidin/green), nucleus (SYTOX/cyan) and YAP expression (red), zoom-in, 25x magnification. Quantification of the fraction of YAP(+) cells (I) and YAP localization measured as the ratio of nuclear to cytoplasmic expression (J). Bar plots show the mean and standard deviation of n = 6 fields of view containing multiple cells (I) and of n = 10 representative single cells from MMPscr vs. noDeg regions (J). Statistical significance with Kruskall-Wallis and Dunn's correction in (E, F) and with ANOVA and Bonferroni correction in (I, J) (***/ ### = $p < 0.001$, with * for comparison of materials and # for comparison of time points). Scale bar: 500 µm (A, B), 20 µm (G, H).